PHYSICS OF OUR DAYS

Experimental studies of two-dimensional complex plasma crystals: waves and instabilities

L Couëdel, V Nosenko, S Zhdanov, A V Ivlev, I Laut, E V Yakovlev,
N P Kryuchkov, P V Ovcharov, A M Lipaev, S O Yurchenko

Contents

Abstract. A review of experimental studies on waves, phonon dispersion relations, and mode-coupling instability in two-dimensional complex plasma crystals is presented. An improved imaging method allowing simultaneous measurements of the three wave modes (compression in-plane, shear in-plane, and out-of-plane) is given. This method is used to evidence the formation of hybrid modes and the triggering of the mode-coupling instability due to wake-mediated interactions. The main stages of the mode-coupling instability are analyzed. In the early stages, synchronization of microparticle motion at the hybrid mode frequency is reported. The spatial orientation of the observed synchronization pattern correlates well with the directions of the maximal increment of the shear-free hybrid mode. When the instability is fully developed, a melting front is formed. The propagation of the melting front has similarities with flame propagation in ordinary reactive matter. Finally, it is experimentally demonstrated that an external mechanical excitation of a stable 2D complex plasma crystal can trigger the mode-coupling instability and lead to the full melting of a two-dimensional complex plasma crystal.

L Couëdel [1,2,a], **V Nosenko** [3], **S Zhdanov** [3], **A V Ivlev** [4], **I Laut** [3],
E V Yakovlev [5], **N P Kryuchkov** [5], **P V Ovcharov** [5], **A M Lipaev** [6],
S O Yurchenko [5,b]
[1] Physics and Engineering Physics Department,
   University of Saskatchewan,
   Saskatoon, S7N 5E2, Saskatchewan, Canada
[2] CNRS, Aix Marseille Univ.,
   PIIM, UMR 7345, 13397 Marseille 20, France
[3] Institut für Materialphysik im Weltraum,
   Deutsches Zentrum für Luft- und Raumfahrt,
   D-82234 Weßling, Germany
[4] Max Planck Institute for Extraterrestrial Physics,
   D-85741 Garching, Germany
[5] Bauman Moscow State Technical University,
   ul. 2-ya Baumanskaya 5/1, 105005 Moscow, Russian Federation
[6] Joint Institute for High Temperatures, Russian Academy of Sciences,
   ul. Izhorskaya 13/19, 127412 Moscow, Russian Federation
E-mail: [a] lenaic.couedel@usask.ca, [b] st.yurchenko@mail.ru

1. Introduction

Complex plasmas consist of particles immersed in weakly ionized gas-discharge plasmas [1–4]. Because of the absorption of ambient electrons and ions, microparticles acquire significant (negative) charges and can form strongly coupled systems analogous to conventional soft matter (complex fluids). In ground-based experiments, calibrated microparticles injected into capacitively coupled radio-frequency (cc-rf) discharges levitate at the same height and form a monolayer in the sheath region near the bottom electrode, where the electric field can balance gravity. Under certain conditions, the monolayer arranges itself into an ordered structure: a 2D complex plasma crystal.

2D complex plasmas are particularly convenient systems for detailed experimental studies of generic phenomena in strongly coupled systems (liquids and crystals) at the atomic level. The essential advantage is that one can obtain complete information about the state of the whole system of particles in the kinetic $(\mathbf{x}, \mathbf{v})$-space. This offers an important benefit for the investigation of fluctuation spectra [5–8], pair correlations [9, 10], and collective processes occurring in strongly coupled media, including melting and recrystallization [11–14], diffusion and heat transport [15], and solitons and shocks [16].

In 2D complex plasma crystals, as in any (strongly coupled) 2D system, two in-plane wave modes with an

acoustic dispersion can be sustained (longitudinal-compression and transverse-shear modes). Since the strength of the vertical confinement is finite, there is also a third fundamental wave mode associated with out-of-plane oscillations [16–21]. Theory predicts that this mode has a negative (or inverse) optical dispersion [21].

Since the microparticles composing a 2D complex plasma crystal levitate in the sheath above the electrode, they are subject to a strong ion flow coming from the bulk plasma. In the presence of this strong ion flow, the screening cloud around each charged particle becomes highly asymmetric. These downstream elongated ion clouds, which are usually referred to as 'plasma wakes' [22–24], play the role of an (external) 'third body' in interparticle interactions and, hence, make it nonreciprocal [25, 26]. The nonreciprocity of pair interaction in complex plasmas provides a very efficient mechanism for converting the energy of the flowing ions into the kinetic energy of microparticles [3, 4, 25]. In particular, dust-lattice (DL) wave modes [17, 21, 27] can contribute to that. The microparticle kinetic energy can grow due to resonant particle-wake interactions when different oscillation modes are properly synchronized: the crystal in-plane and out-of-plane modes couple into a shear-free hybrid mode of the lattice layer and trigger mode-coupling instability (MCI) [19, 21, 28, 29], which can melt the crystal [30–32]. Localized 'hot spots' in the lattice phonon spectra are a typical signature of the hybrid mode [21, 29]. MCI-induced melting can only be triggered if (i) the modes intersect, and (ii) neutral gas damping is sufficiently low [29].

Wake-induced mode coupling is also possible in liquid complex plasma monolayers [33]. However, in this case, the confinement and dust particle density thresholds, which are important features of MCI in 2D complex plasma crystals, disappear, and the instability has a higher growth rate. Consequently, conditions exist for which both the crystalline and the fluid states are viable, meaning no crossing of the modes in the crystal state and an MCI growth rate high enough in the fluid state to prevent crystallization. This explains why, in many experiments, the crystallization of a monolayer is achieved only by increasing the gas pressure and/or the rf power (confinement strength is an increasing function of the discharge power [34]) well above the melting threshold. In addition, it is, in principle, possible to trigger sporadic melting of a stable crystal which is not too far from the crystalline MCI threshold by applying a sufficiently strong mechanical perturbation.

In this review, experimental results of the past decade on dedicated studies of wave modes and mode-coupling instability in 2D complex plasma crystals are presented. The experimental set-up is described in Section 2. Section 3 is dedicated to the presentation of an experimental technique allowing the measurement of the spectra of phonons with out-of-plane polarization in 2D plasma crystals. An improved method of particle imaging was developed and used to resolve particle motion in three dimensions and measure simultaneously the in-plane and out-of-plane wave spectra [27]. In Section 4, we report on the experimental observation of the coupling between the out-of-plane mode and the in-plane longitudinal mode which can form hybridized modes and trigger MCI [30, 35]. In Section 5, the kinematics of dust particles during the early stage of MCI is explored. It is demonstrated that the formation of the hybrid mode induces the partial synchronization of particle oscillations at the hybrid frequency [36, 37]. Phase- and frequency-locked hybrid particle motion in both the vertical and horizontal directions is evidenced. In Section 6, the later stages of MCI and the propagation of the melting front are carefully analyzed. It is found to be similar to the propagation of a flame front in ordinary matter [32]. In Section 7, an example of externally forced MCI melting is presented. Finally, in Section 8, the main results are summarized.

2. Experimental set-up

Experiments were carried out in a cc-rf glow discharge at 13.56 MHz (modified GEC chamber). A diagram of the set-up is presented in Fig. 1. The argon pressure p_{Ar} was between 0.4 Pa and 1 Pa and the forward rf power P_{RF} was between 5 W and 20 W. In the bulk discharge, the electron temperature was $T_e = 2.5$ eV and the electron density was $n_e = 2 \times 10^9$ cm^{-3} at $p_{Ar} = 0.66$ Pa and $P_{RF} = 20$ W [38]. Melamine-formaldehyde spherical particles with a diameter of 9.19 ± 0.09 μm were levitated in the plasma sheath above the lower rf electrode and formed a horizontal monolayer up
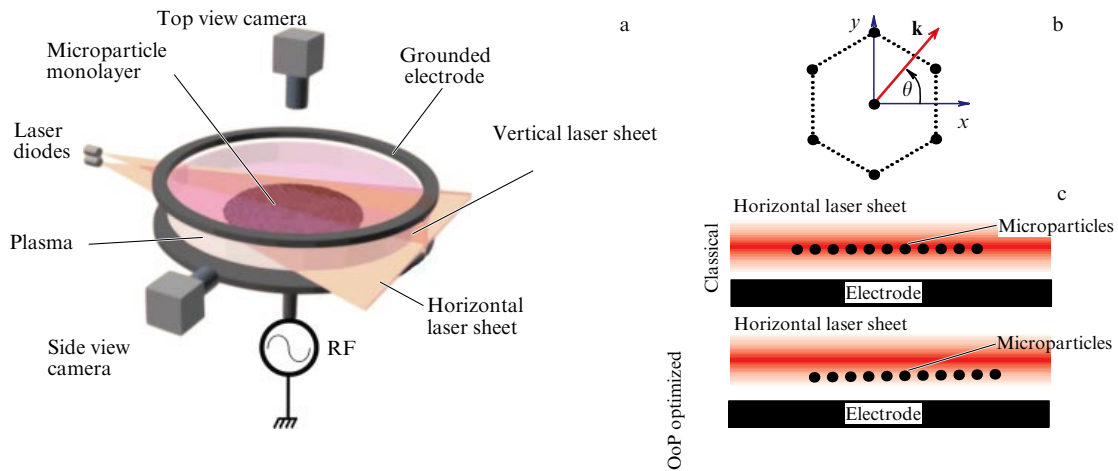
Figure 1. (Color online.) (a) Schematic of the experimental set-up. (b) An elementary cell of the hexagonal lattice and the frame of reference chosen in this article. The orientation angle θ of the wave vector **k** is measured with respect to the x-axis. (c) Position of the laser sheet for particle tracking in the conventional (top) and out-of-plane motion optimised (bottom) configurations, enabling the study of the out-of-plane fluctuation spectra (see Fig. 2).

to ~ 60 mm in diameter. The microparticles were illuminated by a horizontal laser sheet which had a Gaussian profile in the vertical direction with a standard deviation $\sigma \simeq 75$ μm (corresponding to full width at half maximum of ~ 175 μm). The sheet thickness was approximately constant across the whole crystal. The particles were imaged through a window at the top of the chamber by a Photron FASTCAM camera at a speed of 250 frames per second. The particle horizontal coordinates, x and y, and velocities, v_x and v_y, were then extracted with sub-pixel resolution in each frame. An additional side-view camera (Basler Ace ACA640-100GM or Photron FASTCAM camera) was used to check that we were indeed working with a single layer of particles. More details can be found in previous publications [27, 29–31, 39, 40].

3. Measurement of in-plane and out-of-plane waves

To explore the wave properties of the microparticle monolayer, tracking data are used to compute the particle velocity fluctuation spectra. First, the particle current components $V_s(\mathbf{k}, t)$ are obtained:

$$V_s(\mathbf{k}, t) = \sum_{j=1}^{N} v_{s,j}(t) \exp\left[-i\mathbf{k}\,\mathbf{s}_j(t)\right]. \tag{1}$$

They are calculated in the s-direction at the time moment t, using a wave vector $\mathbf{k} = \{k_x, k_y\}$ located in the horizontal plane. Here, i is the imaginary unit, j is the particle index, $v_{s,j}(t)$ is the s-projection of the j-th particle velocity, $\mathbf{s}_j = \{x_j, y_j, z_j\}$ is its position, and N is the number of microparticles. Note that axes x and y are chosen as shown in Fig. 1(b). Fixing the axis directions allows us to easily choose the direction of the wave propagation with respect to the lattice principal axis. A fast Fourier transform in the time domain is then implemented to obtain the current fluctuation spectra.

The horizontal coordinates x and y and the corresponding velocities v_x and v_y can be extracted from the video frames using standard techniques [41, 42]. The in-plane current fluctuation spectra can thus be directly computed. In Fig. 3, the resulting fluctuation spectra are shown for two principal orientations of the wave vector, at $\theta = 0$ and $30°$. The spectra represent the wave energy distribution in the $(f, \mathbf{k})$ space, so that the 'ridge' of this distribution yields the wave dispersion relation.

However, in order to extract the vertical position z and velocity v_z of individual particles, we needed to employ a very different technique [27]. Unlike relatively compact Coulomb clusters, where these values can be directly measured by using the side view, the particles forming large monolayers cannot be individually resolved from the side. Therefore, the out-of-plane particle tracking can only be performed by using the top view, and then the vertical displacement should be deduced from the relative variation in scattered light intensity.

Particles are normally imaged by adjusting the laser light sheet position, such that the peak of the Gaussian intensity profile practically coincides with the particle monolayer levitation height (see Fig. 1c). This 'conventional' method facilitates the in-plane tracking, especially at high frame rates. It is, however, not appropriate to obtain z and v_z. Indeed, the variation in particle image intensities between consecutive frames gives only the magnitude of the vertical displacement. The direction of displacement stays undefined. As a matter of fact, the intensity of the individual particle image in each

frame is proportional to the local illumination intensity:

$$I(z) \propto \exp\left[-\frac{(z - z_{\max})^2}{2\sigma^2}\right], \tag{2}$$

where $z_{\max}$ is the position of the intensity maximum. When the mean levitation height z_{lev} is very close to $z_{\max}$, the magnitude of the particle displacements $|\delta z|$ can greatly exceed $|z_{\mathrm{lev}} - z_{\max}|$. Moreover, positive or negative displacement can give the same variation in image intensity [16]. The 'conventional' method has another issue associated with its sensitivity. Since $\delta z|z_{\mathrm{lev}} - z_{\max}|$, the resulting intensity variations scale as $\delta I/I \approx (1/2)(\delta z/\sigma)^2$. Assuming that the vertical displacement is due to thermal fluctuations, its magnitude $|\delta z|$ is roughly $|\delta z| \sim (T_{\mathrm{d}}/m_{\mathrm{d}} \Omega_{\mathrm{v}}^2)^{1/2} \lesssim 10$ μm, where T_{d} is the kinetic temperature of particles, m_{d} is their masses, and $\Omega_{\mathrm{v}} = 2\pi f_{\mathrm{v}}$ is the resonance frequency in their vertical confinement. This value is much smaller than the standard deviation $\sigma \approx 75$ μm of the laser sheet intensity in the vertical directions. The relative intensity variations are thus at the level of $\delta I/I \sim 1$, making them hardly detectable.

In our experiments, an alternative out-of-plane motion-optimized method of particle visualization was developed [27]. The microparticles were levitated ~ 100 μm below the position of the maximum intensity of the laser light sheet, giving $|z_{\mathrm{lev}} - z_{\max}|/|\delta z| \approx 10$. This gave us two advantages compared to the 'conventional' method:

1. Particles move in the region where the vertical intensity gradient is positive. Consequently, there is no ambiguity in the direction of displacement.

2. The relative intensity variations scale almost linearly with the displacement, $\delta I/I \approx |z_{\mathrm{lev}} - z_{\max}|\delta z/\sigma^2$, giving $\delta I/I$, about 15 times larger than the one the 'conventional' tracking method.

It is worth noting that the quality of the tracking in the horizontal xy plane is not critically affected when compared to the 'conventional' tracking configuration. However, different background intensities for the in-plane and out-of-plane spectra are observed.

The recovered fluctuation spectra of out-of-plane waves using the 'conventional' and the alternative method are shown in Fig. 2. As can be seen, the use of the 'conventional' method (Fig. 2a) leads to spectra containing very little to no
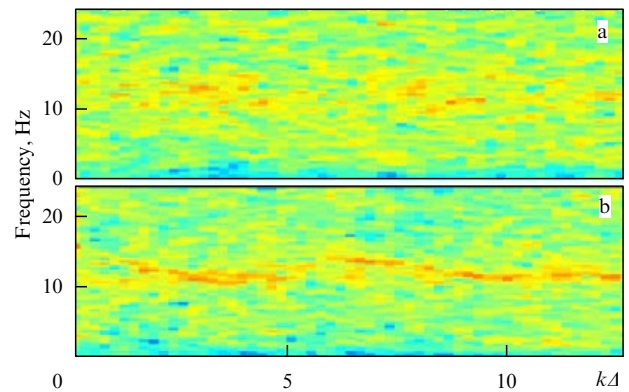
Figure 2. (Color online.) Example of out-of-plane current fluctuation spectra. (a) Using scattered light intensity from an unshifted laser sheet (conventional method). (b) Using scattered light intensity from a shifted laser sheet (out-of-plane optimized method). In both cases, the analyzed crystal area was a mixture of different crystal orientations.
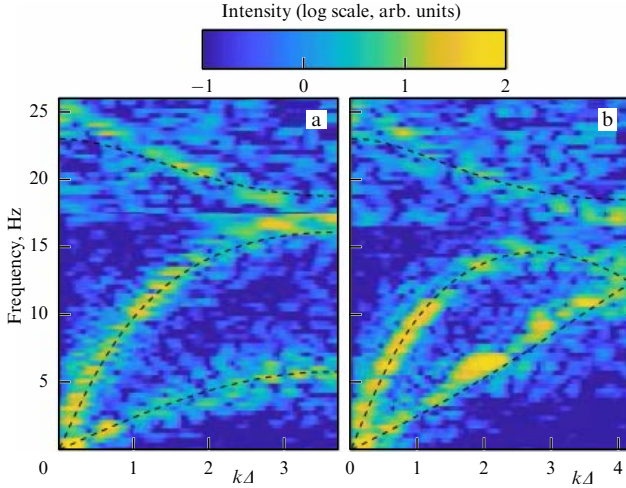
Figure 3. (Color online.) Comparison of the experimentally measured dust-lattice dispersion relations with theory. In-plane and out-of-plane current fluctuation spectra deduced from the experiments (see Table) and the theoretical curves are shown. The results are presented for two directions of the wave vector $\mathbf{k}$ for (a) $\theta = 0$ and (b) $\theta = 30°$ (see Fig. 1). The dashed lines are the theoretical dispersion relations for a pure Yukawa interaction between particles [21]. The shown range of $\mathbf{k}$ is limited by the first Brillouin zone ($|\mathbf{k}|\varDelta = 2\pi/\sqrt{3}$ for $\theta = 0$ and $|\mathbf{k}|\varDelta = 4\pi/3$ for $\theta = 30°$). Note the different background intensities for the in-plane and out-of-plane spectra induced by the alternative tracking method.

information about the out-of-plane wave modes. On the contrary, the alternative method (Fig. 2b) reveals the out-of-plane dispersion relation (ridges in the intensity distribution).

The alternative method allows us to measure all three wave modes of a 2D plasma crystal in a single experimental run. In Fig. 3, the out-of-plane current fluctuation spectrum is plotted simultaneously with the in-plane spectra for two major crystal orientations, $\theta = 0$ and $30°$, in the first Brillouin zone. The lines represent the theoretical dispersion relations, which depend on the particle charge number Z_d and the lattice screening parameter $\kappa = \varDelta/\lambda_D$, where $\varDelta$ is the interparticle distance and λ_D the effective (Debye) screening length. The parameters were deduced from the in-plane fluctuation spectra using the following approach, inspired from Ref. [43].

The interactions between microparticles in complex plasmas are primarily determined by the Yukawa (screened-Coulomb) potential $\varphi(r)$:

$$\varphi(r) = \frac{Z_d^2 e^2}{4\pi\varepsilon_0} \frac{\exp(-r/\lambda_D)}{r}, \tag{3}$$

where ε_0 is the electric constant, r is the distance between two microparticles, and Z_d is given in units of the elementary charge e. The lattice screening parameter κ can be determined by fitting the long wavelength part ($|\mathbf{k}\varDelta| \leqslant 1$) of the experimental in-plane fluctuation spectrum with the theoretical dispersion relation [21, 29] for a two-dimensional

Table. Parameters of the 2D crystal used for the spectra shown in Fig. 3. The lattice constant $\varDelta$ is obtained from the position of the first peak of the pair correlation function. Parameters Z_d and κ are deduced from the in-plane phonon spectra.

P_{RF}, W	p_{Ar}, Pa	Z_d, e	$\varDelta$, μm	κ	f_v, Hz
20	0.42	21,000±3000	550±20	1±0.25	25±2

triangular lattice of Yukawa particles. In particular, the acoustic in-plane modes are determined as [21]

$$\Omega_{h\pm}(\mathbf{k}) = \sqrt{\alpha_h \pm \sqrt{\beta^2 + 4\gamma^2}},$$

$$\alpha_h = \sum_{m,n} \exp(-K)(K^{-1} + K^{-2} + K^{-3}) \sin^2 \frac{1}{2}\mathbf{ks}, \tag{4}$$

$$\beta = \sum_{m,n} \exp(-K)(K^{-1} + 3K^{-2} + 3K^{-3})\left(\frac{s_y^2 - s_x^2}{s^2}\right)\sin^2\frac{1}{2}\mathbf{ks},$$

$$\gamma = \sum_{m,n} \exp(-K)(K^{-1} + 3K^{-2} + 3K^{-3})\left(\frac{s_x s_y}{s^2}\right)\sin^2\frac{1}{2}\mathbf{ks},$$

where $K = \kappa\sqrt{m^2 + n^2 + mn}$, m, n are integer numbers. The $\pm$ sign in Eqn (4) corresponds to a pair of acoustic in-plane (longitudinal and transverse) modes. The vector $s_x = (\sqrt{3}/2)m$ with component $s_y = (1/2)m + n$ characterizes the positions of all particles in the hexagonal lattice. Note that the wavevector $\mathbf{k}$ in Eqn (4) is normalized as $\mathbf{k}\varDelta \rightarrow \mathbf{k}$, and all frequencies are normalized by the dust lattice (DL) frequency

$$\Omega_{DL} = \sqrt{\frac{(Z_d e)^2}{M\lambda_D^3}}, \tag{5}$$

where M is the mass of a particle.

The values of Z_d and κ, obtained using this method for the spectra shown in Fig. 3, are listed in the Table. All dispersion curves calculated using the obtained values and the theory of Ref. [21] are also plotted. Pure Yukawa interactions (no ion wakes) were assumed to calculate the theoretical dispersion curves. As can be seen, the experimental spectra are in good qualitative agreement with the theoretical dispersion curves. In-plane and out-of-plane DL wave branches are clearly visible. The out-of-plane measurements revealed the optical character of the out-of-plane dispersion relation (the frequency of the long-wavelength waves is nonzero). Moreover, it showed that the dispersion at long wavelengths is negative (the wave frequency decreases as the wave number increases). At larger $|\mathbf{k}|$, the wave dispersion is different for $\theta = 0°$ and $30°$. The small differences between the theoretical curves and the measurements arise from the chosen interparticle potential.

4. Hybrid modes
## in two-dimensional complex plasma crystals

When the in-plane longitudinal mode and the out-of-plane mode cross, the formation of an unstable hybrid mode is theoretically predicted due to the nonreciprocity of the dust particle pair interactions [19, 21, 28, 29]. This can under specific conditions trigger MCI and melt the 2D complex plasma crystal. This behavior was first reported experimentally in Ref. [30]. Two different scenarios were used to trigger melting:

1. A gradual decrease in rf power at a constant gas pressure (which lowers f_v; Ref. [34]).

2. A decrease in pressure at a constant rf power (which naturally lowers neutral gas friction and modifies the radial confinement and hence $\varDelta$).

In either case, the melting developed in the same way [30–32]: upon a decrease in the control parameter below a certain threshold, MCI was triggered in the central part of the crystal where the particle density was the highest and then expanded
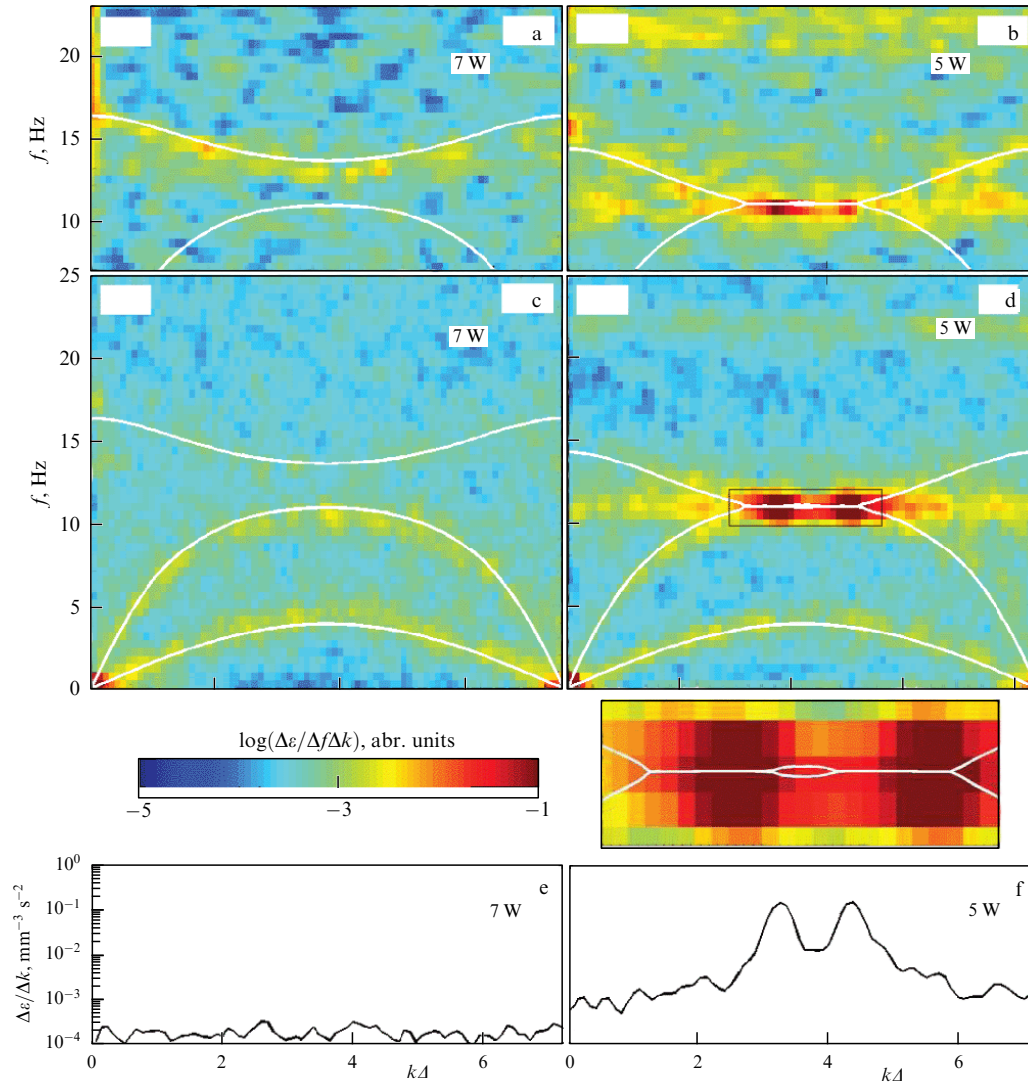
Figure 4. (Color online.) From Ref. [30]. Evolution of the DL dispersion relations near the instability onset. The dispersion relations ('fluctuation spectra') were measured in the experiment performed at an argon pressure of 0.76 Pa with particles 9.19 μm diameter, at an rf power of 7 W (left column, stable regime) and 5 W (right column, instability onset). The logarithmic color coding is used for the 'fluctuation intensity' $\Delta\varepsilon/\Delta k \, \Delta f$ (energy density, for unit mass, per unit wave number and frequency): yellow ridges represent stable wave modes, the unstable hybrid mode are the dark red 'hot spots'; (a) and (b) show the measured out-of-plane mode, (c) and (d) depict the pair of in-plane modes. The solid lines on (a)–(d) are theoretical results [21] (see text for details). The wave number k is normalized by the inverse interparticle distance Δ^{-1}. The shown range of k corresponds to the first two Brillouin zones at $\theta = 0$ (branches are symmetric with respect to the border between the two zones). Below the fluctuation spectra the magnified hybrid mode in the unstable regime (marked by a rectangular box) is shown. (e) and (f) illustrate the distribution of the 'fluctuation energy' $\Delta\varepsilon/\Delta k$ at a fixed frequency: in the stable case, the frequency ($\simeq 12.5$ Hz) is chosen in the middle between the longitudinal in-plane branch and the out-of-plane branch (measured at the border between the Brillouin zones); for the instability onset the frequency ($\simeq 11$ Hz) corresponds to the hybrid mode.

outwards. The development of MCI always occurs simultaneously in the horizontal and vertical directions [30, 36]. At the initial stage, an exponential growth of the particle kinetic energy was reported [32, 40], eventually resulting in the total disruption of the crystalline order. Since MCI always operates in 2D complex plasma fluid [33], the system recrystallizes when increasing the control parameters well above the threshold of MCI in the crystal (strong hysteresis) [29, 44]. If the rf power is sufficiently high and/or the particle density in the monolayer is low enough, the crystal remains stable at practically any pressure.

In this section, it is shown that the reported melting behavior imputable to MCI fully agrees with the qualitative picture given by the MCI theory [21]. The qualitative effects and features of MCI, originally predicted by the theory for a 1D string [19, 28, 45], all remain unaltered in the 2D case as well. The distinctive fingerprint of MCI [19, 45] is the crossing of the longitudinal in-plane and transverse out-of-plane DL branches, resulting in wake-induced resonance coupling between them. An unstable *hybrid mode* consequently emerges in a certain proximity of the crossing. This effect was experimentally demonstrated by measuring the dispersion relations of all three principal DL modes [29, 30, 46, 47].

In Fig. 4, we present the results of the first direct observation of MCI [30]. The theoretical curves show all principle modes that fit the frequency range shown. Since theory predicts the orientation $\theta = 0$ to be the most unstable [21] (see Fig. 1), the fluctuation spectra shown in Fig. 4 were plotted for the wave vector **k** at $\theta = 0$. In the left column of Fig. 4, the wave modes are well separated and the fluctuation

intensity is evenly distributed over the branches. It corresponds to the stable regime. On the contrary, in the right column of Fig. 4 there is an apparent intersection between the out-of-plane and the longitudinal in-plane branches. The intersection occurs in the vicinity of the first Brillouin zone boundary. The dark red spots in the spectra are a clear indication of the anomalous energy release due to MCI. This is the unstable regime.

The theoretical results for 2D crystals obtained by Zhdanov et al. [21] were used for comparison with the experimental data. The theoretical branches are shown in Fig. 4 by solid lines. A normalized dipole moment of the wake $\tilde{q}\tilde{\delta} = 0.1$ (where $\tilde{q}$ is the normalized wake charge and $\tilde{\delta}$ is the normalized wake spatial extent; see Ref. [21] for the full definitions) was used for the calculation. Yukawa interparticle interactions were assumed.

As can be seen, Fig. 4 shows that the theory yields excellent agreement with the experiment, for both the stable and unstable regimes. Especially important is the fact that in the unstable regime (right column) the calculated unstable hybrid mode perfectly matches with the locations of 'hot spots' in the measured fluctuation spectra. Even subtle effects, such as the splitting of 'hot spots' at the border between the Brillouin zones, is very well resolved (see the distribution of the fluctuation energy in Fig. 4e, f, and also the magnified hybrid mode). Also note the traces of mixed polarization in Fig. 4d (traces of the out-of-plane mode are visible in the in-plane spectrum close to the hybrid mode). These results prove the existence of the unstable hybrid mode triggering MCI. However, it is worth noting that the MCI triggering observes thresholds in confinement strength and neutral damping rate [29]. The strength of the ion wake, as well as the wake model used, also plays a role in determining the thresholds. More details can be found in Refs [29, 48–50].

5. Early stage of mode-coupling instability: particle motion synchronization

The formation of the hybrid mode often triggers MCI (if the gas pressure is low enough so that the energy input due to the unstable hybrid mode exceeds neutral damping). At the early stages of MCI, the development of rhythmic patterns and synchronized oscillations of the microparticles around their equilibrium positions has been observed [32, 36, 40]. The first dedicated experiments devoted to the study of the development of dust oscillation synchronization during the early stages of MCI were presented in Ref. [36]. In this article, the kinematics of dust particles during the early stages of MCI in the plasma crystal were explored. The instability was initiated by decreasing the argon pressure from $p_{Ar} = 0.94$ Pa to 0.92 Pa at fixed forward rf power $P_{RF} = 12$ W. The longitudinal and transverse sound speeds, respectively $C_L = (34.1 \pm 1.4)$ mm s^{-1} and $C_T = (7.9 \pm 0.3)$ mm s^{-1}, were measured by using the long wavelength part ($k \to 0$) of the longitudinal and transverse in-plane spectra (see Fig. 2 of Ref. [36]). The interparticle separation in the center of the crystal was found to be $\Delta = 480 \pm 10$ μm. Following the method proposed in Ref. [43], the charge of the dust particles $|Z_d| = 18{,}600$ and the coupling parameter $\kappa = 1.26$ were calculated. The error in the charge was about 15% and the error in κ was about 30%. The frequency of the vertical particle oscillations (the 'vertical confinement parameter') $f_v = 23 \pm 1$ Hz was extracted from the out-of-plane fluctuation spectrum. The hybrid mode, showing up as a hot spot at

the frequency $f_{hyb} = 16 \pm 1$ Hz, was well pronounced in the longitudinal velocity fluctuation spectrum (Fig. 2 of Ref. [36]).

During the first instant of MCI, synchronized oscillations of the microparticles around their equilibrium positions were observed. The microparticle trajectories were used to quantify the degree of synchronization. The instantaneous phases of the particle trajectories as functions of time and position were recovered from the particle displacements $r_j(t) = (x_j^2(t) + y_j^2(t))^{1/2}$. The drift was removed to keep only the oscillatory parts. The 'filtered' displacement $\tilde{r}_j(t)$ of the jth particle was defined as

$$\tilde{r}_j(t) = r_j(t) - \frac{1}{\Delta t} \int_{t-\Delta t/2}^{t+\Delta t/2} r_j(t') \, \mathrm{d}t' , \qquad (6)$$

where Δt, the interval of averaging, was chosen to be the same, $\Delta t = 0.5$ s, for all $j = 1 \ldots N$. A Hilbert transform was then applied to obtain the analytical signal $r_{aj}(t) = A_j(t) \exp(\mathrm{i}\phi_j(t))$, where $\phi_j(t)$ are instantaneous phases and $A_j(t)$ is the instantaneous amplitude [51].

The degree of synchronization σ_j between the particle j and its closest neighbors was then calculated as follows [52]:

$$\sigma_j = \frac{1}{n} \sum_{j'=1}^{n} \sigma_{jj'} , \qquad (7)$$

$$\sigma_{jj'} = 1 - \frac{S_{jj'}}{S_{max}} , \qquad (8)$$

where n is the number of the closest neighbors, and $S_{jj'}$ is the Shannon entropy of the cycle phase distribution between neighbors,

$$S_{jj'} = -\sum_{l=1}^{M} p_{jj'l} \ln p_{jj'l} , \quad \sum_{l=1}^{M} p_{jj'l} = 1 . \qquad (9)$$

Here, $p_{jj'l}$ is the fraction of the data in the l-th bin in the distribution of phase differences $\phi_{jj'}(t) = \phi_j(t) - \phi_{j'}(t)(\mathrm{mod}\, 2\pi)$, $l = 1 \ldots M$, $M = 20$ is the number of bins, and $S_{max} = \ln M$ is the maximum entropy corresponding to a uniform distribution $p_{jj'l} = M^{-1}$. A moving window using the instantaneous phases $\phi_{jj'}(t)$ calculated for 101 consecutive frames centered on time t was used to compute the distribution. A completely synchronized state corresponds to $\sigma = 1$, while a fully desynchronized state corresponds to $\sigma = 0$.

In Fig. 5a, the trajectories of two neighbor particles during the early stage of MCI are presented. As can be seen, they oscillated at the hybrid frequency in both the vertical and horizontal planes. Since the hybrid mode has both an in-plane and out-of-plane component, this is a signature of the hybrid mode, which locks the particle motion in both phase and frequency. As observed in Fig. 5b and c, the system self-organizes in a rhythmic pattern of alternating in-phase and anti-phase oscillating chains of particles. The interpenetrating antiphase oscillating 'sublattices' are illustrated in Fig. 5b. In Fig. 5c, rows of the in-phase (synchronized) oscillating particles can be seen. As MCI develops, more particles become involved, enlarging the synchronization pattern. Neighboring rows of the synchronically oscillating particles move almost in anti-phase. In the experiment reported in Ref. [36], the motion of the synchronically moving particles was strongly 'polarized' in the $\theta = 60°$ direction. This spatial orientation correlated well with the directions of the maximal increment of the shear-free hybrid mode. Since the hybrid mode has a wave number $k = k_{hyb}$ close to $k\Delta = k_{hyb}\Delta = \pi$, it explains the quasi anti-phase oscillation of particles belonging to neighboring rows. Indeed, the jth particle oscillations
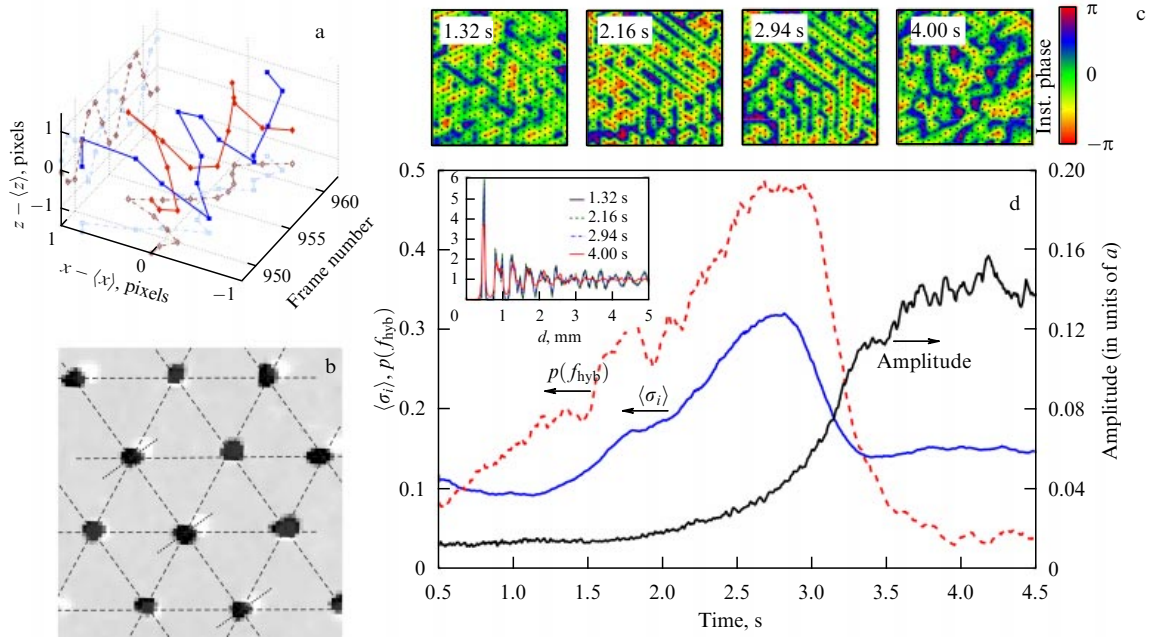
Figure 5. (Colour online.) From Ref. 36: (a) trajectories of two neighboring particles [red (plain diamond symbols) and blue (plain square symbols) plain lines] exhibiting a periodic motion at the hybrid frequency $f_{hyb} \simeq 16.5 \pm 0.8$ Hz in both the vertical and horizontal directions. The dashed light-blue (unfilled square symbols) and light-red (unfilled diamond symbols) lines are the projection on the (x, t) and (z, t) planes. (b) Two superposed images of the lattice layer separated in time by a half period ($\Delta t \simeq 0.032$ s). The absolute time moment, $t \simeq 2.7$ s, was taken close to the maximum of the synchronization index (see Fig. c). The white and black dots represent the particle positions. The mean interparticle separation in the chosen region is $\Delta = 470 \pm 16$ μm. Three sets of parallel dashed lines are shown to guide the eye. The stacked images were shifted along the main deformation direction to graphically demonstrate the character of the particle vibrations. The main deformation direction is as the dotted lines indicate. Note that in this direction the lattice is about 7–9% more compact. Importantly, the distance between the in-phase oscillating rows of particles is kept nearly constant. (c) Consecutive snapshots (a 300×300-pixel area of the original video) indicating the instantaneous phase distribution for desynchronized phase states (the very left and right images, $t = 1.32$ s and $t = 4.00$ s) and during the synchronization state (two middle images, $t = 2.16$ s and $t = 2.94$ s). Black dots show the position of the particles. (d) Evolution of the cumulative probability $p(f_{hyb})$ (red dashed curve) of finding a particle with an instantaneous frequency in the band $14 < f < 18$ Hz around f_{hyb}, the mean value of the synchronization index σ (averaged over particles, solid blue curve), and the averaged instantaneous amplitude of particle oscillations (solid black curve). In performing the averaging, about 150 particle tracks at the center of the crystal (a 145×145-pixel area of the original video) were taken into account. The inset shows the radial pair correlation functions taken at the indicated time moments.

are proportional to $\exp(i\mathbf{k}\mathbf{r}_j)$ and, consequently, at $k = k_{hyb}$ the motion of neighboring particles should obviously be almost anti-phase. Moreover, when MCI is triggered, only oscillations associated with the hybrid mode have a growth rate surpassing the damping rate. All other wave modes tend to equilibrate with the surrounding gas discharge. Therefore, the hybrid mode accumulates energy, resulting in an exponential growth of the amplitude of the corresponding hybrid mode oscillations. Any motion related to other modes sustained in the crystal is consequently hidden. By making a second order Taylor expansion of the force between two neighboring particles, it can be shown that a coupling between the phases of in-plane and out-of-plane motion of neighboring particles exists. Yet oscillators with any phase-dependent interaction can evolve until their phases are (partially) synchronized [53]. Furthermore, since the shear in-plane component of the hybrid mode is very weak, rows of particles belonging to equivalent elementary cells must have synchronized motion. When the amplitude of motion is too large, the crystalline order is destroyed, and the synchronization naturally vanishes (see Fig. 5d). The melted zone nevertheless expands to the whole monolayer due to the existence of fluid MCI [33].

It should, however be noted that the synchronization pattern should develop in all equivalent directions of the maximal increment of the shear-free hybrid mode. Experi-

mentally, however, this is rarely the case [36, 37]. The observed break of symmetry could be explained by crystal deformation (compression) due to small asymmetries in the horizontal confining potential [37, 54] and has been confirmed theoretically [55] and numerically [37, 54]. Crystal compression leads to an asymmetric formation of the hybrid mode and anisotropic triggering of mode-coupling instability.

6. Mode-coupling induced melting

As stated in the introduction, nonreciprocal wake-mediated interactions can trigger the MCI in both crystalline [19, 21, 29, 56] and fluid [33, 40, 57] complex plasmas. As shown in Section 4, the necessary condition for the onset of instability is a crossing of the out-of-plane and longitudinal in-plane wave modes, leading to the formation of an unstable hybrid mode and a rapid increase in particle kinetic energy. In crystals, at a given strength of the vertical confinement, a density threshold exists that needs to be exceeded to trigger MCI. This is the reason why experimentally MCI starts in the central densest region of the crystal, provided that the crystal parameters are right for the crossing of the longitudinal in-plane mode and the out-of-plane mode. In contrast, in a fluid complex plasma monolayer, the modes always cross [33]. Consequently, there are no density or confinement thresholds, and a fluid MCI can exist, while under the same

conditions a crystalline monolayer would be stable (no crossing of the modes). This explains why in many experiments the melting expands to the whole monolayer once MCI is triggered at (and only at) the center of the monolayer. Hence, heat activation of a stable monolayer complex plasma crystal can provide a direct analogy with activation in ordinary reactive matter.

In this section, we present a detailed study of the propagation of melting front in a complex plasma monolayer as reported in Ref. [32]. Crystalline MCI was triggered at a pressure of 1 Pa and rf power of 20 W. Under these conditions, MCI, triggered in the central region, expanded outward. In order to understand the evolution of the melted area in the crystal, Voronoi triangulation was performed and the bond-orientational order parameter Ψ_6 was calculated for each cell,

$$\Psi_6 = \frac{1}{N_{nn}} \sum_{j=1}^{N_{nn}} \exp\left(6i\theta_j\right), \tag{10}$$

where N_{nn} is the number of nearest neighbors and θ_j is the bond angle for the jth neighbor. The kinetic temperature of particles (the thermal part of particle kinetic energy) was obtained by subtracting the collective motion due to acoustic fluctuations from the velocity field:

$$T = \frac{m_d}{2} \sum_i \left(\mathbf{v}_i - \langle \mathbf{v}_i \rangle\right)^2, \tag{11}$$

where $\mathbf{v}_i$ is the instantaneous in-plane velocity of the ith particle, and $\langle \mathbf{v}_i \rangle$ is the instantaneous average velocity of all particles in the vicinity of radius 2Δ to 3Δ around the ith particle (e.g., we used 2.4Δ to obtain the results shown in Refs 12 and 13). One should note that the size of the analysis area is directly related to the concept of a physically small volume [58]. On the one hand, the choice of a small analysis area (with very few particles) is preferable to show in detail the spatial distribution of some parameters (e.g., fields of velocity, density, thermal and hydrodynamic parts of energy). However, in this case, large fluctuations of the parameters will be observed due to the poor statistics. On the other hand, the choice of too large an area suppresses fluctuations, but leads to artificial and unphysical smoothing of the calculated fields. During the analysis of our experiments, a compromise was reached when the radius of the averaging ranged from 2Δ to 3Δ, providing results in agreement with each other.

To complement the experiments, molecular dynamics (MD) simulations were also performed (details about MD can be found in Appendix B of Ref. [32]).

The evolution of the kinetic temperature is shown in Fig. 6a. After a slight decrease in rf discharge power resulting in a reduction in the vertical confinement below the crystalline MCI threshold, crystalline MCI sets in. In the central region, the kinetic energy rapidly grew and the crystalline order was destroyed. Then, as reported in other studies [40], the melting expanded outward, completely destroying the crystal. The
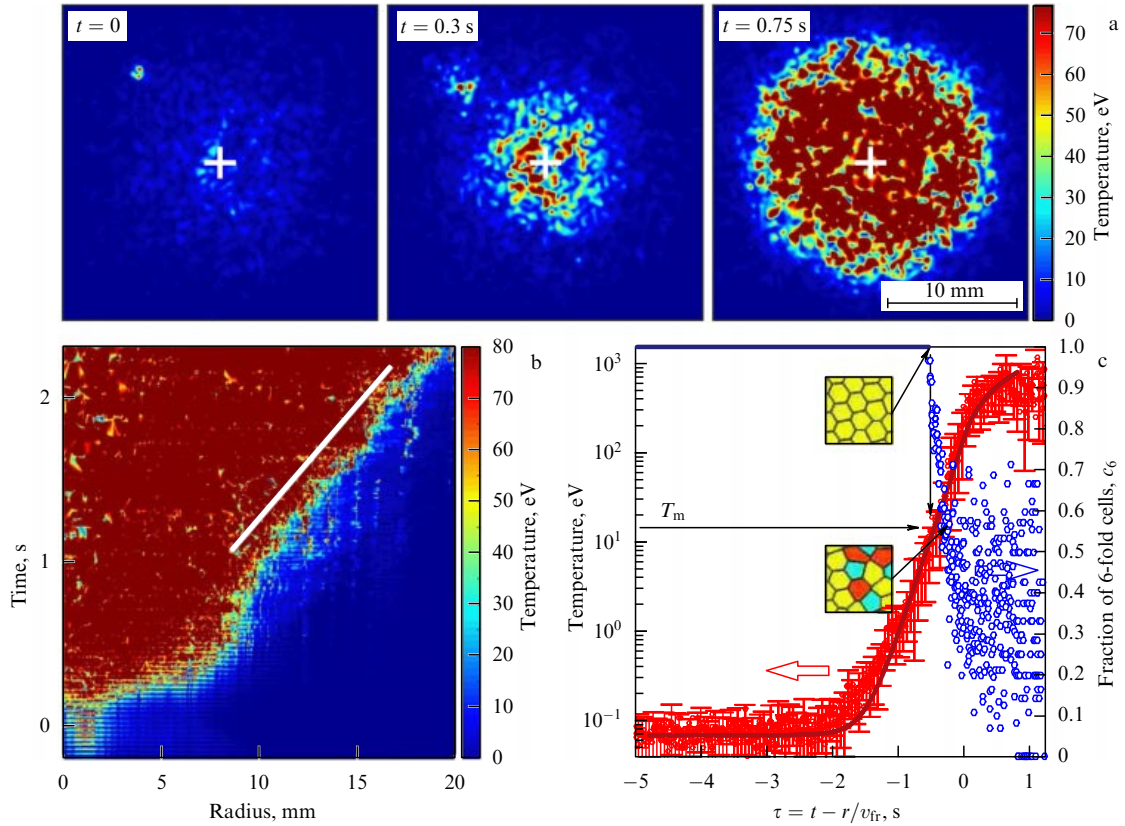
Figure 6. (Color online.) From Ref. 32. (a) Typical evolution of the microparticle kinetic temperature during MCI-induced melting (top view). Crystalline MCI triggers melting of the central region, then the melting expands outward in the form of a sharp front, supported by intense heating behind the front due to fluid MCI. (b) Radial expansion of the hot zone with time. At $t \sim 1$ s, the ignition phase due to the crystalline MCI changes to a steady expansion sustained due to fluid MCI (indicated by the white solid line). (c) Self-similar profiles of the particle kinetic temperature $T(\tau)$ (left axis) and of the fraction of sixfold cells $c_6(\tau)$ (right axis). The symbols are experimental results, and the solid line is a fit to Eqn 14. The insets are color-coded snapshots of the Voronoi diagram near the flame front: sixfold cells are yellow, while five- and sevenfold cells are blue and red, respectively.
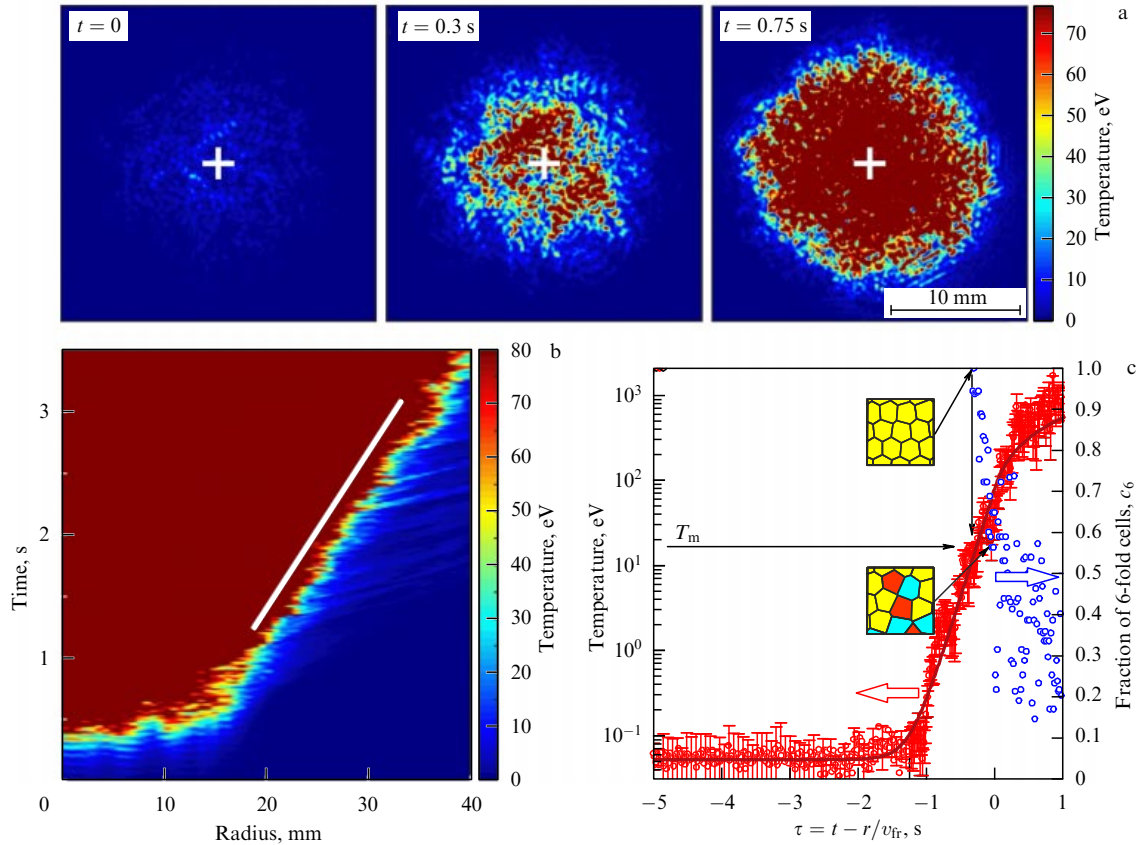
Figure 7. (Color online.) Molecular dynamics simulations. Same caption as Fig. 6.

propagating melting front ('flame' front) was very sharp and propagated steadily due to the energy input from fluid MCI [33]. Behind the front, the kinetic temperature exceeded that in the crystalline region by ~ 3 orders of magnitude. The same behavior could be reproduced in MD simulations. For instance, in Fig. 7a, a similar sharp interface and a strong temperature gradient are also observed. In Figs 7a and b, the formation of the flame front is detailed. First, oscillating horizontal stripes were seen in the initial (ignition) phase. They are a typical fingerprint of crystalline MCI (see previous section and Ref. [36]). In the region of crystalline MCI, the kinetic energy of the microparticles rapidly grew, and when the amplitudes of the oscillations of the microparticles were too large, the crystal melted. This initial melting rapidly developed into a hot zone with a sharp boundary expanding outward at a constant radial velocity. In Ref. [32], the front velocity was $v_{fr} = 7.0 \pm 0.2$ mm s^{-1}. Note that at the periphery of the crystal, in which the hot zone expanded, the equilibrium particle density was noticeably lower (up to $\sim 25\%$) preventing any crystalline MCI. This undoubtedly shows the activation of fluid MCI at the hot zone front edge. It was recently shown that ignition and full melting of the crystal can also be triggered by other means than crystalline MCI, such as local laser heating [59], a rapidly moving particle under the monolayer [35], or external mechanical excitation (see Section 7). The formation of the front follows a similar evolution in simulations (Figs 7b and c).

Analogies between flame front propagation in conventional reactive matter and MCI-induced melting can be found. Indeed, the evolution of the spatial temperature distribution $T(r, t)$ in a continuous reactive medium can be represented by the following heat equation [32, 60]:

$$\frac{\partial T}{\partial t} = \frac{Q(T)}{Cn} + \chi\left(\frac{\partial^2 T}{\partial r^2} + \frac{D-1}{r}\frac{\partial T}{\partial r}\right), \qquad (12)$$

where $Q(T)$ is the reaction heat rate of the medium (of the spatial dimension D), χ is the thermal diffusivity, n is the number density, and C is the isobaric heat capacity per particle. As the melting zone expands, the second term in parentheses tends to 0, reducing the problem to one dimension.

The chemical kinetics in a given reactive medium determine the heat source $Q(T) \propto \exp\left(-E_A/T\right)$ for Arrhenius-like chemical activation, with E_A the activation energy. A critical heat phenomenon, such as ignition or explosion, generally depends on the particular feature of $Q(T)$, which can be a complex function [61]. In our case (steady "flame" propagation), the temperature varies rapidly across the front making the features of $Q(T)$ of minor importance. Only its behaviors at low and high temperatures play an important role. $Q(T)$ is thus routinely approximated by the Heaviside step function in the theory of combustion and flames [61]. In our case, the fluid MCI heat source can be described as [32]

$$\frac{Q(T)}{Cn} = \begin{cases} 0, & T < T_*, \\ q_\infty, & T > T_*, \end{cases} \qquad (13)$$

where T_* is the activation temperature at which the unstable hybrid mode forms, triggering fluid MCI. The maximum heating is estimated as $q_\infty = \gamma(T_\infty) T_\infty/C$, where

$T_\infty \approx 1$ keV is the saturation temperature of the fluid MCI [33] and $\gamma(T)$ is the (temperature-dependent) growth rate of the instability. Since the vertical confinement strength is finite, the heat capacity of the 2D fluid complex plasma is in the range $C = 2 \ldots 3$ [62]. By solving Eqns. (12) and (13), a self-similar solution to the temperature profile across the front can be found [32, 63]:

$$\frac{T(\tau) - T_0}{T_* - T_0} = \begin{cases} \exp\left(\dfrac{\tau v_{\mathrm{fr}}^2}{\chi}\right), & \tau < 0, \\[2ex] 1 + \dfrac{\tau v_{\mathrm{fr}}^2}{\chi}, & \tau > 0, \end{cases} \tag{14}$$

where $\tau = t - r/v_{\mathrm{fr}}$ is the self-similar time and v_{fr} is the front velocity, related to the activation temperature via $T_* - T_0 = q_\infty \chi / v_{\mathrm{fr}}^2$. Regimes $\tau \lessgtr 0$ represent, respectively, a nonactivated crystalline state preheated by thermal diffusion ('inert zone') and a state with developed fluid MCI ('reactive' zone) [61]. Due to neutral gas damping, an additional term, $-2\gamma_{\mathrm{d}}(T - T_0)/C$, should normally be present on the right-hand side of Eqn (12), where T_0 is the equilibrium temperature in the absence of heating and γ_{d} is the Epstein damping rate (for our experimental conditions, $\gamma_{\mathrm{d}} \simeq 1.2$ s^{-1}). However, the damping can be ignored if the growth rate v_{fr}^2/χ is much larger than $2\gamma_{\mathrm{d}}/C$.

The experimental self-similar profile $T(\tau)$ was obtained by averaging the thermal part of the particle kinetic energy at different radial distances from the center of the hot zone. The fraction of six-fold Voronoi cells, $c_6(\tau)$, was also calculated to detect the onset of melting. Figure 6c presents the results of the analysis.

The equilibrium temperature $T_0 = 0.07 \pm 0.04$ eV was obtained from the averaging of the data points far from the melting front ($\tau \leqslant -2.5$ s in Fig. 6c). The temperature grows exponentially in the crystal (where c_6 is close to unity) when approaching the 'flame' front. When the melting sets in, c_6 starts decreasing (see snapshots of the Voronoi diagram in Fig. 6c). The melting occurs at ~ 14 eV, which agrees with the predicted equilibrium melting temperature T_{m} of a 2D Yukawa crystal [64, 65], given the experimental values of κ and Z_{d}. The fit to Eqn (14) (solid line) was then obtained by using the least-squares method with varying activation temperature T_*, growth rate v_{fr}^2/χ, and position of the activation point $\tau = 0$. This yields $T_* = 160 \pm 15$ eV and $v_{\mathrm{fr}}^2/\chi = 5.1 \pm 0.1$ s^{-1} ($> 2\gamma_{\mathrm{d}}/C \sim 1.2$ s^{-1}, justifying the fact that of neutral damping was disregarded). The heat diffusivity was then obtained: $\chi \simeq 9.6$ mm^2 s^{-1}. This value agrees with previous measurements of the thermal diffusivity [15]. Figures 6c and 7c demonstrate excellent agreement among the experimental, simulated, and theoretical temperature profiles.

In concluding this section, we have demonstrated experimentally and numerically that MCI operating in 2D complex plasmas reveals all the essential features of combustion, such as activated heat release and the two-zone structure of the self-similar temperature profile ('flame' front). The presented results are of relevance for various fields, ranging from combustion and thermochemistry, to chemical physics and synthesis of materials.

7. Externally forced mode-coupling instability

As already explained, wake-induced mode coupling is possible in both crystalline and liquid complex plasmas [33].

However, in complex plasma liquids, confinement and dust particle density thresholds, which are important features of MCI in 2D complex plasma crystals, disappear, and the instability growth rate is higher. In the previous section, it was thus shown that fluid MCI explains the propagation of the melting to the whole complex plasma monolayer.

In this section, we show experimentally that wake-mediated resonant mode coupling can be induced in a 2D plasma crystal levitating in the sheath of a radio-frequency discharge by means of an external mechanical excitation mechanism. When the excitation is strong enough, it can trigger MCI and the melting of the 2D complex plasma crystal.

In this experiment, a stable 2D crystal (no crossing of the eigenmodes and thus no crystal MCI) was levitated above the electrode ($p_{\mathrm{Ar}} = 0.94$ Pa, $|Z_{\mathrm{d}}| \approx 1.8 \times 10^4$, $\varDelta = 490 \pm 20$ μm, and $\kappa \approx 1.2$). The measured in-plane longitudinal fluctuation spectrum of the crystalline layer is shown in Fig. 8a. No fingerprints of the unstable hybrid mode could be detected, and only the eigenmodes (natural waves) are present. A kick (mechanical excitation) was then applied to the bottom of the vacuum chamber near the powered electrode.

The vibrations were transmitted to the microparticle monolayer, and in return the microparticles started to oscillate both vertically and horizontally around their equilibrium positions with amplitudes much higher than natural thermal oscillations. The crystal also oscillated horizontally as a whole. However, the respective mean velocity was subtracted before computing the mean kinetic energy and current spectra. In Fig. 8b, the in-plane longitudinal fluctuation spectrum after mechanical excitation is plotted. As can be seen, a bright spot emerges at $\simeq 28$ Hz.

The resulting second subharmonic oscillations at $\simeq 14$ Hz induce resonant coupling with the eigenmode at $k\varDelta \simeq 2.3$ (subharmonics are commonly observed for large amplitude oscillations in complex plasmas [66, 67]). Traces of mixed polarization (branches corresponding to the out-of-plane mode in the in-plane spectrum) are visible close to the edge of the first Brillouin zone (yellow spots at $k\varDelta \lesssim 3.63$) and are a clear fingerprint of mode hybridization and MCI onset.

In Fig. 8d, the evolutions of the average kinetic energy of dust particles is plotted. In order to demonstrate the evolution of the crystalline symmetry, we also plot the average bond-orientational order $\langle |\varPsi_6| \rangle$ [see Eqn (10)]. The kinetic temperature started to increase exponentially just after the kick, with a measured growth rate $\gamma_{\mathrm{cryst}} = 1.4 \pm 0.1$ s^{-1}. At $t = 0.4$ s, the melting began in the center, reflected by a rapid fall-off of $\langle |\varPsi_6| \rangle$, and the growth rate simultaneously increased to $\gamma_{\mathrm{liq}} = 5.8 \pm 0.1$ s^{-1}.[1] This behavior indicates a transition from the crystalline to the liquid regime of the MCI, as predicted in Ref. [33], and is very similar to the results reported in Section 6. Correlated oscillations of E_{kin} and $|\varPsi_6|$ are due to partially synchronized motions of the microparticles in the crystalline domains [36].

This experiment clearly demonstrates that in undercritical crystals (stable against crystalline MCI), if a mechanical perturbation is strong enough, hybridization can be forced and the crystal can undergo melting (as in regular MCI).

---

[1] During the meting phase, the mean interparticle distance remained constant to an accuracy of 0.25 pixels.
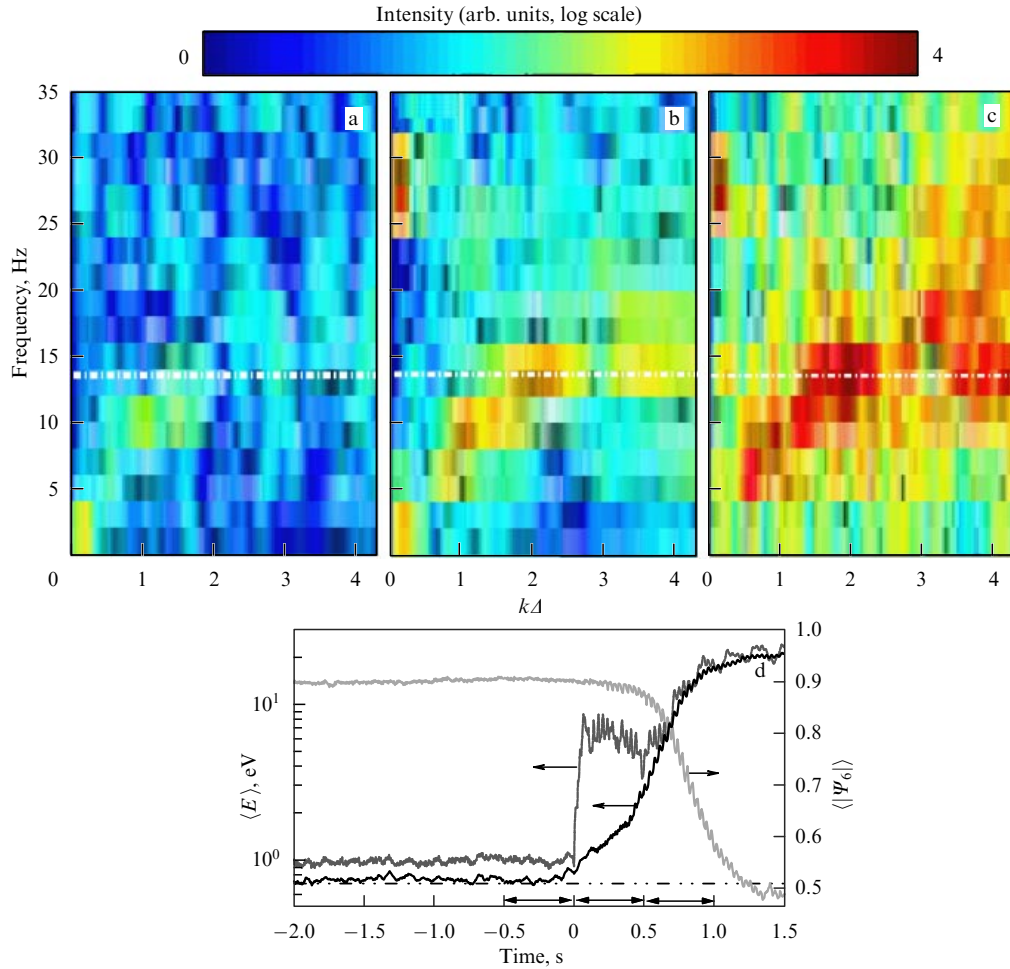
Figure 8. (Color online.) Forced mode-coupling instability, induced by mechanical excitation. The in-plane longitudinal fluctuation spectra in (a), (b), and (c) are obtained for the time intervals indicated in (d) by the respective arrows. Only the in-plane longitudinal eigenmode is observed before the excitation (a), while after knocking the chamber (at time $t = 0$), a bright spot emerges at $\simeq 28$ Hz (c). The resulting second subharmonic oscillations at $\simeq 14$ Hz (horizontal dotted line) induce resonant coupling with the eigenmode at $k\Delta \simeq 2.3$. The crystal in this experiment is composed of several domains with different orientations; therefore, the shown range of k is limited by the border of the first Brillouin zone at $\theta = 30°$. (d) Evolutions of the (averaged) in-plane kinetic energy with mean velocity (dark grey), without mean velocity (black) and $\langle|\Psi_6|\rangle$ (light grey) in the experiment. The horizontal dashed-dotted line shows the mean energy level before the excitation. Note the increase in the exponential energy growth rate and the simultaneous decrease in $\langle|\Psi_6|\rangle$, occurring at $t \simeq 0.4$ s due to the transition from the crystalline to liquid regime of the mode-coupling instability. For technical reasons, the dynamics of particles with $E_{kin} \gtrsim 10$ eV cannot be properly followed, which causes artificial saturation of $\langle E\rangle(t)$.

8. Conclusion

In this review, experimental studies on waves, phonon dispersion relations, and mode coupling instability in 2D complex plasma crystals were presented. An improved imaging method of 2D complex plasma monolayers allowing the simultaneous measurement of the three wave modes was discussed. This method was then used to evidence the formation of hybrid modes and the triggering of mode coupling instability due to the presence of ion wakes. The different stages of the mode coupling instability were then carefully analyzed. In the early stages of a weak instability, synchronization of the microparticle motion at the hybrid mode frequency was reported. The spatial orientation of the synchronization pattern correlated well with the directions of the maximal increment of the shear-free hybrid mode. When the instability was fully developed, the analysis of the propagation of the melting front revealed a remarkable analogy with flame propagation in ordinary reactive matter. Finally, it was shown that an external mechanical excitation of a stable 2D complex plasma crystal can also trigger the

coupling of the modes and lead to the melting of the complex plasma monolayer. In future investigations, wave dispersion measurements will be used to extract quantitative information about the ion wakes and obtain a quantitative estimation of the mode-coupling instability growth rate.

The physics of 2D systems has attracted significant interest in recent times [68, 69]. The fundamental and applied significance of the relevant studies is caused by the ubiquitous presence of 2D many-body systems in nature, e.g., in atomic monolayers [70–73], thin molecular films on different substrates [74–76], electrons and ions trapped on surfaces and at interfaces [77, 78], vortices in thin-film semiconductors [79–81], colloidal particles at flat interfaces and on surfaces [82–87], and complex (dusty) plasmas in ground-based conditions [32, 57, 88]. 2D systems exhibit a rich diversity of phase transitions and peculiarities of collective fluctuations and transport phenomena, owing to the enhanced role of long-range fluctuations and anharmonicity (see Refs [44, 65, 83, 89–92] and references therein). However, most previous studies were performed for near-equilibrium cases, while nonequilibrium behavior still remains poorly understood.

Due to their openness, 2D complex (dusty) plasmas serve as systems with a tunable thermal activation behavior, which offers unique opportunities for future interdisciplinary studies of nonequilibrium generic phenomena in plasma-related soft matter systems.

References

1. Morfill G E, Tsytovich V N, Thomas H *Plasma Phys. Rep.* **29** 1 (2003); *Fiz. Plazmy* **29** 3 (2003)
2. Fortov V E et al. *Phys. Usp.* **47** 447 (2004); *Usp. Fiz. Nauk* **174** 495 (2004)
3. Fortov V E et al. *Phys. Rep.* **421** 1 (2005)
4. Morfill G E, Ivlev A V *Rev. Mod. Phys.* **81** 1353 (2009)
5. Kryuchkov N P et al. *Sci. Rep.* **9** 10483 (2019)
6. Kryuchkov N P, Brazhkin V V, Yurchenko S O *J. Phys. Chem. Lett.* **10** 4470 (2019)
7. Brazhkin V V *Phys. Usp.* **60** 954 (2017); *Usp. Fiz. Nauk* **187** 1028 (2017)
8. Brazhkin V V *Phys. Usp.* **62** 623 (2019); *Usp. Fiz. Nauk* **189** 665 (2019)
9. Yakovlev E V et al. *J. Chem. Phys.* **151** 114502 (2019)
10. Klumov B A *Phys. Usp.* **53** 1053 (2010); *Usp. Fiz. Nauk* **180** 1095 (2010)
11. Melzer A, Homann A, Piel A *Phys. Rev. E* **53** 2757 (1996)
12. Melzer A et al. *Phys. Rev. E* **54** R46 (1996)
13. Thomas H M, Morfill G E *Nature* **379** 806 (1996)
14. Schweigert V A et al. *Phys. Rev. Lett.* **80** 5345 (1998)
15. Nosenko V et al. *Phys. Rev. Lett.* **100** 025003 (2008)
16. Samsonov D, Zhdanov S, Morfill G *Phys. Rev. E* **71** 026410 (2005)
17. Vladimirov S V, Shevchenko P V, Cramer N F *Phys. Rev. E* **56** R74 (1997)
18. Vladimirov S V, Yaroshenko V V, Morfill G E *Phys. Plasmas* **13** 030703 (2006)
19. Ivlev A V, Morfill G *Phys. Rev. E* **63** 016409 (2000)
20. Qiao K, Hyde T W *Phys. Rev. E* **68** 046403 (2003)
21. Zhdanov S K, Ivlev A V, Morfill G E *Phys. Plasmas* **16** 083706 (2009)
22. Vladimirov S V, Nambu M *Phys. Rev. E* **52** R2172 (1995)
23. Vladimirov S V, Ishihara O *Phys. Plasmas* **3** 444 (1996)
24. Ishihara O, Vladimirov S V *Phys. Plasmas* **4** 69 (1997)
25. Melzer A, Schweigert V A, Piel A *Phys. Rev. Lett.* **83** 3194 (1999)
26. Ivlev A V et al. *Phys. Rev. X* **5** 011035 (2015)
27. Couëdel L et al. *Phys. Rev. Lett.* **103** 215001 (2009)
28. Yaroshenko V V, Ivlev A V, Morfill G E *Phys. Rev. E* **71** 046405 (2005)
29. Couëdel L et al. *Phys. Plasmas* **18** 083707 (2011)
30. Couëdel L et al. *Phys. Rev. Lett.* **104** 195001 (2010)
31. Williams J D et al. *Phys. Rev. E* **86** 046401 (2012)
32. Yurchenko S O et al. *Phys. Rev. E* **96** 043201 (2017)
33. Ivlev A V et al. *Phys. Rev. Lett.* **113** 135002 (2014)
34. Steinberg V et al. *Phys. Rev. Lett.* **86** 4540 (2001)
35. Couëdel L et al. *Europhys. Lett.* **115** 45002 (2016)
36. Couëdel L et al. *Phys. Rev. E* **89** 053108 (2014)
37. Laut I et al. *Europhys. Lett.* **110** 65001 (2015)
38. Nosenko V et al. *Phys. Plasmas* **16** 083708 (2009)
39. Couëdel L et al. *Phys. Rev. Lett.* **109** 175001 (2012)
40. Röcker T B et al. *Europhys. Lett.* **106** 45001 (2014)
41. Rogers S S et al. *Phys. Biol.* **4** 220 (2007)
42. Feng Y, Goree J, Liu B *Rev. Sci. Instrum.* **78** 053704 (2007)
43. Nunomura S et al. *Phys. Rev. Lett.* **89** 035001 (2002)
44. Kryuchkov N P, Ivlev A V, Yurchenko S O *Soft Matter* **14** 9720 (2018)
45. Ivlev A V et al. *Phys. Rev. E* **68** 026405 (2003)
46. Liu B, Goree J, Feng Y *Phys. Rev. Lett.* **105** 085004 (2010)
47. Liu B, Goree J, Feng Y *Phys. Rev. Lett.* **105** 269901 (2010)
48. Röcker T B et al. *Phys. Plasmas* **19** 033708 (2012)
49. Röcker T B et al. *Phys. Plasmas* **19** 073708 (2012)
50. Röcker T B et al. *Phys. Rev. E* **89** 013104 (2014)
51. Menzel K O, Arp O, Piel A *Phys. Rev. E* **83** 016402 (2011)
52. Toth R, Taylor A F *J. Chem. Phys.* **125** 224708 (2006)
53. Kuramoto Y *Chemical Oscillations, Waves, and Turbulence* (Berlin: Springer-Verlag, 1984)
54. Laut I et al. *Phys. Rev. E* **93** 013204 (2016)
55. Ivlev A V et al. *Phys. Rev. E* **91** 063108 (2015)
56. Yakovlev E V et al. *Phys. Rev. E* **100** 0230203 (2019)
57. Kryuchkov N P et al. *Phys. Rev. Lett.* **121** 075003 (2018)
58. Lifshitz E M, Pitaevskii L P *Physical Kinetics* (Oxford: Pergamon Press, 1981); Translated from Russian: *Fizicheskaya Kinetika* (Moscow: Nauka, 1979)
59. Couëdel L et al. *Phys. Rev. E* **97** 043206 (2018)
60. Landau L D, Lifshitz E M *Fluid Mechanics* 2nd ed. (Oxford: Pergamon Press, 1987); Translated from Russian: *Gidrodinamika* 4th ed. (Moscow: Nauka, 1988)
61. Zeldovich Ya B et al. *The Mathematical Theory of Combustion and Explosions* (New York: Consultants Bureau, 1985); Translated from Russian: *Matematicheskaya Teoriya Goreniya i Vzryva* (Moscow: Nauka, 1980)
62. Dove M T *Introduction to Lattice Dynamics* (Cambridge Topics in Mineral Physics and Chemistry, Vol. 4) (Cambridge: Cambridge Univ. Press, 1993)
63. Ivlev A et al. *Astrophys. J.* **805** 59 (2015)
64. Hartmann P et al. *Phys. Rev. E* **72** 026409 (2005)
65. Kryuchkov N P, Khrapak S A, Yurchenko S O *J. Chem. Phys.* **146** 134702 (2017)
66. Nosenko V et al. *Phys. Rev. Lett.* **92** 085001 (2004)
67. Nunomura S et al. *Phys. Rev. E* **68** 026407 (2003)
68. Ryzhov V N et al. *Phys. Usp.* **60** 857 (2017); *Usp. Fiz. Nauk* **187** 921 (2017)
69. Ryzhov V N et al. *Phys. Usp.* DOI: https://doi.org/10.3367/UFNe.2018.04.038417, in preparation; *Usp. Fiz. Nauk* DOI: https://doi.org/10.3367/UFNr.2018.04.038417, in preparation
70. Kim J H et al. *J. Phys. D* **52** 083001 (2018)
71. Wang S, Robertson A, Warner J H *Chem. Soc. Rev.* **47** 6764 (2018)
72. Wang H et al. *Adv. Mater.* **30** 1704382 (2018)
73. Lin C-Y et al. *ACS Nano* **11** 11015 (2017)
74. Gu Z-G, Zhang J *Coord. Chem. Rev.* **378** 513 (2019)
75. Becchi M, Giuntoli A, Leporini D *Soft Matter* **14** 8814 (2018)
76. Zhang Y et al. *J. Chem. Phys.* **149** 184902 (2018)
77. Levin Y, Flores-Mena J E *Europhys. Lett.* **56** 187 (2001)
78. Yurchenko S O et al. *Langmuir* **32** 11245 (2016)
79. Guillamón I et al. *Nature Phys.* **5** 651 (2009)
80. Hoffmann A et al. *Phys. Rev. B* **77** 060506(R) (2008)
81. Jing Z, Yong H, Zhou Y *Supercond. Sci. Technol.* **31** 055007 (2018)
82. Grimes C C, Adams G *Phys. Rev. Lett.* **42** 795 (1979)
83. Khrapak S A et al. *J. Chem. Phys.* **149** 134114 (2018)
84. Pieranski P *Phys. Rev. Lett.* **45** 569 (1980)
85. Kelleher C P et al. *Phys. Rev. E* **92** 062306 (2015)
86. Aveyard R et al. *Phys. Rev. Lett.* **88** 246102 (2002)
87. Garbin V et al. *Phys. Rev. Lett.* **114** 108301 (2015)
88. Mikikian M et al. *Phys. Rev. Lett.* **105** 075002 (2010)
89. Khrapak S A, Kryuchkov N P, Yurchenko S O *Phys. Rev. E* **97** 022616 (2018)
90. Khrapak S *AIP Adv.* **8** 105226 (2018)
91. Khrapak S, Klumov B, Couëdel L *Sci. Rep.* **7** 7985 (2017)
92. Semenov I L, Khrapak S A, Thomas H M *Phys. Plasmas* **22** 114504 (2015)